Electrochemical control of the morphology and functional properties of hierarchically structured, dendritic Cu surfaces

Authors: Hamed Mehrabi,[1] Samuel K. Conlin,[2] Thomas I. Hollis,[2] Brayley S. Gattis,[2] Johanna Nelson Weker,[3] Robert H. Coridan[1,2*]

[1] Materials Science and Engineering Program, University of Arkansas, Fayetteville, AR, 72701, USA

[2] Department of Chemistry and Biochemistry, University of Arkansas, Fayetteville, AR, 72701, USA

[3] Stanford Synchrotron Radiation Lightsource, SLAC National Accelerator Laboratory, Menlo Park, California 94025, United States

* rcoridan@uark.edu

Abstract

Electrodeposited dendritic copper foams have been extensively studied as an electrocatalyst for CO_2 reduction reaction (CO_2RR). Many parameters, such as dendrite size, porosity, pore size, and crystal faceting, define the hierarchical properties of these structures and their subsequent bubble evolution and CO_2RR capabilities. Here we studied the effects the electrodeposition conditions (potential, pH) have on the resulting crystallinity, microstructure, and macroporosity of the copper foam. We characterized these morphological differences and the corresponding effects on electrocatalytic activity. We showed that the composition of the electrodeposition bath can have significant effects on the mechanics of bubble formation and detachment at the surface during hydrogen evolution reaction (HER) in acidic solutions. Similarly, the electrodeposition conditions for the synthesis of the foam affected the product selectivity during CO_2RR electrocatalysis. Foams deposited in alkaline electrodeposition solutions showed high faradaic efficiency and specificity towards C_2H_6, an uncommon product of CO_2RR, at modest applied potentials (-0.8 V vs. RHE).

Keywords: CO_2 reduction, hierarchical structure, electrocatalysis, transmission x-ray microscopy, morphology

Complex functional composites often rely on the multiscale organization of various functional subunits to generate a specific overall functionality or to maximize the potential performance of the target function. Many studies have focus on the use of these design schemes in for energy conversion and storage, including semiconductor-based photocatalytic CO_2 reduction.[1–3] However, it is also relevant to the operation of simple, structured materials of a single component. For example, natural and synthetic photonic materials generate optical resonances based on the average microscopic periodicity of dielectric contrast while necessitating structure at macroscopic length scales to provide mechanical integrity and robustness.[4] Many natural structures such as butterfly wings and beetle carapaces have been shown to have hierarchical structure that generates macroscopic function such as tailorable camouflage or moisture collection.[5–8] Multiscale structures are of interest in electrocatalysis for similar reasons. A structured electrode can significantly increase the ratio of electrochemically active surface area compared to the projected surface area. This can lower practical electrocatalytic overpotentials to improve the viability of earth-abundant or non-precious metal-based electrocatalysts.[9] Intentionally chosen structure for electrocatalytic interfaces can also allow them to be integrated into multifunctional materials without deleterious effects on other function. An example is the patterning of an electrocatalyst layer to minimize reflection, parasitic absorption, and impairing the photovoltage-generating effects of a semiconductor-liquid junction.[10,11] The structure of the material induces heterogeneities in the environment at the electrocatalyst interface that can influence the resulting chemical reactions. For example, the electrode structure affects the diffusion layer and local pH in a nanostructured electrode, influencing the product distribution during electrochemical CO_2 reduction.[12–14]

A common approach to fabricating hierarchically structured metallic interfaces is high-rate electrodeposition. At low deposition rates, the solution near the interface maintains a sufficient

local concentration of reducible metal ions to allow for the deposition of conformal coatings. Increasing the deposition rate reduces the local concentration of ions at the interface to the point where the deposition is limited by mass transport kinetics. This phenomenon is known as diffusion-limited aggregation.[15] Under higher current densities, the local growth morphology can be influenced by anisotropic surface energies, resulting in electrochemical control over branching and deposition kinetics.[16] Heterogeneous dendritic structures can be formed under these conditions, which results in an interface with characteristic structure on multiple length scales, and correspondingly complex mass transport characteristics. The hierarchical structure of the dendritic interface can therefore be controlled by electrochemical parameters such as the bulk concentration of the metal ion in the electrolyte and the applied electrochemical bias.

Cu electrodeposition is generally performed in highly acidic solutions based on the $Cu^{2+}_{(aq)}/Cu_{(s)}$ equilibrium denoted in the Cu Pourbaix diagram.[17] The abundance of hydronium in these solutions facilitates bubble generation from hydrogen evolution as a competing electrochemical reaction to Cu deposition on the cathode. The two competing reactions affect the morphology of the resultant dendritic foam structures on multiple length scales. The hydrogen bubbling obstructs the available surface for metal deposition, which confines the dendritic growth to regions between the bubbles while creating a system of interconnected voids at the bubble evolution sites. This deposition process is referred to as dynamic hydrogen bubble templating (DHBT).[2,18,19] Many studies have focused on controlling the properties of DHBT foams, particularly on variables such as bath temperature, deposition potential, and the introduction of surfactants that can control bubbling mechanics through modification of the surface tension of the gas-liquid interface.[20] In principle, the effects that bubble evolution have on the surface morphology during Cu electrodeposition can be tailored by increasing the pH of the solution. The reduction potential of the hydrogen evolution reaction (HER) exhibits a Nernstian shift to

more negative potentials with increasing pH.[21] The Pourbaix diagram of copper (Figure S1) shows that Cu^{2+} ions are not stable in aqueous solutions with pH > 7.[17] However, it has been shown that adding lactic acid to solutions can stabilize the copper ion at higher pH. Studies have shown that a Cu^{2+} ion forms a complex with four monodentate lactate ligands, which prevents the spontaneous formation of copper hydroxide in alkaline conditions.[22] Aqueous solutions of lactate-stabilized Cu^{2+} at high pH (9-12) are used for the electrodeposition of Cu_2O in the narrow range of electrode potentials noted by the Pourbaix diagram.[23–26] The Pourbaix diagram also suggests that metallic copper can be deposited at more negative potentials in the same alkaline conditions. Therefore, the electrodeposition of copper in dendritic morphologies is possible at sufficiently negative potentials while mitigating the morphological consequences of DHBT.

Here, we describe the synthesis and functional properties of Cu foam electrodes deposited from alkaline solutions of lactate stabilized Cu^{2+} ions. The copper foams grown at pH 10 (referred to here as base deposited, or BD) showed distinct morphological differences on multiple length scales, including the grain structure of the assembled crystallites, growth direction, surface area-to-mass ratio, and microscale structure when compared to acid deposited (AD) copper foams grown near pH 0. We also characterized the effect that the BD foam electrode structure has on electrochemical function. We observed that the overall structural differences could modify the behavior of electrochemical processes such as the dynamics of hydrogen bubble evolution and the product distribution of the electrochemical CO_2 reduction reaction (CO_2RR). As a result, we show that this chemical control of the Cu foam electrocatalyst synthesis can significantly impact the electrochemical and mass transport properties of the resulting functional interfaces under otherwise identical operando conditions.

Materials

Water (HPLC grade; BDH), methanol (HPLC grade; VWR), acetone (HPLC grade; VWR), and isopropanol (HPLC grade; VWR) were used as received. Copper (II) sulfate pentahydrate (99.99%, Sigma Aldrich), lactic acid (95%; Sigma-Aldrich), sulfuric acid (96%; Sigma-Aldrich), and sodium hydroxide (50% (w/w) in water; Sigma-Aldrich) were used as received. 0.25 mm thickness copper foil (99.9985%; Alfa Aesar) and 0.20 mm thickness nickel foil (99.95%; Alfa Aesar) were used as electrode substrates. For the transmission x-ray microscopy measurements, conventional steel sewing pins with a 30 μm tip diameter were used as electrodes to allow for rotational alignment and single dendrite imaging. All electrochemical potentials were measured using an Ag/AgCl reference electrode (stored in a saturated, aqueous KCl solution; BASi). 0.1 M sodium carbonate decahydrate (99.995%; Sigma-Aldrich) was used as CO_2RR electrolyte. Analytical grade CO_2 (99.999%; Airgas) was used as CO_2 feedstock. For liquid product NMR analysis, 0.500 g of the electrolyte was mixed with 20% w/w D_2O (98%; Sigma-Aldrich) and dimethylsulfoxide (DMSO) (99.98%; Sigma-Aldrich) after CO_2RR experiments. DMSO was used as an internal standard in the NMR spectra.

Methods

Structural characterization of electrodeposited copper foams

X-ray diffraction (XRD) measurements of the electrodeposited copper foams were performed with a Rigaku MiniFlex II diffractometer equipped with a copper anode (λ = 1.54 Å).

The microstructure of the deposited copper foams was imaged using scanning electron microscopy (SEM) (FEI Nova Nanolab 200). Nanometer-scale computed tomography imaging (referred to here as nanoCT) via full-field transmission X-ray microscopy (TXM) was performed using Beamline 6-2C at the Stanford Synchrotron Radiation Lightsource. The energy of incident X-rays (9000. eV) was chosen to be slightly higher than the Cu K-edge (8979 eV) to be

sensitive to small features in the beam path. Tomographic 3D reconstruction on the measured image series (1° rotations, 180 images total) was performed using the TXM Wizard software package.[27] 3D renderings of the resulting reconstructions were generated using the Dragonfly software package (Object Research Systems). Details of the computed tomography methods and analysis are included in the Supporting Information.

Electrodeposition of acid deposited (AD) and base deposited (BD) copper foams

The electrodeposition solution for preparing the AD copper foams consisted of 0.40 M copper (II) sulfate dissolved in an aqueous solution of 1.5 M sulfuric acid. The AD electrodeposition solutions were stable and did not require any pH adjustment before use. The electrodeposition solution for preparing the BD copper foams was made from a starting solution of 0.40 M copper (II) sulfate and 3.0 M lactic acid in water. Concentrated sodium hydroxide solution was added dropwise to the BD Cu foam solution until reaching a pH of 10.0. The pH of the stock alkaline electrodeposition solution was measured prior to each electrodeposition and adjusted to pH 10.0 using small amounts of 1M NaOH. Cu and Ni foil deposition substrates were cut into 25 x 25 mm squares, sanded with 400, 800, and 1000 grit sandpaper, then rinsed with acetone, methanol, isopropyl alcohol, and water in sequence. The cleaned foils were dried using a stream of high purity dry nitrogen.

AD and BD copper foams were electrodeposited using a potentiostat (BioLogic SP-240) in a three-electrode configuration. A 50 cm long, 0.5 mm diameter coiled copper wire (99.995%; Alfa Aesar) was used as the counter electrode, and a Ag/AgCl electrode was used as reference electrode. The working electrode area was a 1.7 cm^2 circle defined by a Viton O-ring. The counter and reference electrodes were placed above the working electrode in the deposition solution. For XRD experiments, AD copper foams were deposited at -2.0V vs. Ag/AgCl for 2 s,

and BD copper foams were deposited at -2.0V vs. Ag/AgCl for 30 s onto nickel foils. These short electrodeposition times were chosen to isolate the early stages of the dendritic growth, the different deposition times for each foam was selected to yield identical masses of deposited copper. The difference in the mass of foil electrodes before and after the foam electrodeposition process shows that the average deposition mass for both acid deposited copper foams (AD Cu) and base deposited copper foams (BD Cu) was 0.4 mg cm^{-2}. The deposited mass cannot be determined directly from electrochemical measurements due to the competitive faradaic hydrogen evolution reaction. After deposition, the foams were rinsed with water and dried with a stream of nitrogen. Ni substrates were used for XRD experiments to unambiguously isolate the diffraction intensity for Cu to the electrodeposited Cu foams.

Cu foil substrates were used for the foams deposited for the purpose of studying electrocatalysis (HER and CO_2RR). This was done to avoid the contribution from contaminant metals to the electrochemical reactions. The AD Cu foam electrocatalysts were deposited at -2.0 V vs. Ag/AgCl for 30 s. The BD Cu foam electrocatalysts were deposited at -2.0 V vs. Ag/AgCl for 720 s. The deposition times were chosen to fabricate larger foams of roughly identical Cu masses. The average deposition mass for both types of foams was 6 mg cm^{-2}. All copper foams were then rinsed with water and dried under dry nitrogen prior to being used for hydrogen evolution studies.

Dendritic Cu foams for nanoCT imaging were prepared by electrodeposition onto the tips of extra-fine steel sewing pins, which facilitated sample rotation for tomographic imaging. Prior to the electrodeposition of dendritic Cu, the pin was coated with an electrodeposited layer of conformal Cu at -0.4 V vs Ag/AgCl for 30 s to ensure that the surface was seeded by a polycrystalline Cu surface before dendrite growth. The tips of the needles were submerged into the deposition electrolyte and then lifted to the point where surface tension created a cone of

solution around the tip. This was done to limit the deposition to the tip of the needle and isolate the initial dendrite growth process. These needle electrodes were deposited at -1.6 V and -2.0 V vs. Ag/AgCl for 0.3 s in the acidic solution and for 2 s in the basic solution, respectively.

Electrochemical characterization of electrocatalytic activity

The hydrogen evolution properties of AD and BD Cu foam electrocatalysts were characterized by galvanostatic hydrogen evolution (-5 mA cm^{-2}) in a 0.1 M sulfuric acid solution. Bubble evolution was measured by imaging bubble growth on the surface of the electrode at 30 fps with a 5x objective lens. We used the same electrochemical cell for the HER bubble evolution experiments that was used for the electrodeposition of the foams (active area = 1.7 cm^2). This geometry enabled the direct imaging of the surface of the working electrode. Four main dynamical properties of each bubbling event were collected from the sequence of images: the location of each bubble's center, the dwell time (the amount of time in seconds the bubble was attached to the surface, from the first frame where the bubble is visible to the frame where the bubble detached from the electrode surface), the moment of separation (the amount of time from the start of electrolysis to the last frame where the bubble is attached to the electrode surface), and bubble diameter at the time of separation. These measurements were performed by extracting frames from the HER recording using the Python package OpenCV [28] then manually analyzing the frames using the microscopy analysis package ImageJ.[29]

For the CO_2RR studies, the foam electrocatalysts were placed in a two-compartment electrochemical cell. An anion exchange membrane (AMVN Selemion; AGC, Inc.) separated the working electrode (WE) compartment the counter electrode (CE) compartment. The reference electrode (RE) was included in the WE compartment. The WE area (0.5 cm^2) was defined by a Viton O-ring. The size of the active area during electrocatalysis was significantly smaller than the area of the foam electrocatalyst as deposited. A 0.1 M Na_2CO_3 solution was used as the

electrolyte in both the WE and CE chambers. CO_2 was continuously bubbled in direct contact to the WE at a rate of 7 sccm via a mass flow controller (S50; Sierra Instruments). The pH of the electrolyte during the continuous flow of CO2 was measured to be 6.8. The CO_2RR experiments were performed at -1.4 V, -1.6 V, and -1.8 V vs Ag/AgCl. These working electrode potentials were calculated to be approximately -0.8 V, -1.0 V, and -1.2 V compared to the reversable hydrogen electrode (RHE) using Equation (1).

	$E_{(RHE)} = E_{(Ag/AgCl)} + 0.197\ V + 0.0592\ V \times pH$	Equation 1

Each chronoamperometry experiment was performed for 90 minutes. The gaseous products of CO_2RR were analyzed every 15 minutes, using gas chromatography (GC; 8610-C with a 2 m Hayesep-D packed column and argon carrier gas; SRI Instruments). The cell gas output was connected to the GC auto sampler with an open loop when not sampling which maintained 1 atm of gas pressure in the cell. The flame ionization detector (FID) equipped with a methanizer was used to quantify the concentration of CO, CH_4, C_2H_4, and C_2H_6 and thermal conductivity detector (TCD) were used to quantify the concentration of H_2 in the headspace. The gas products were analyzed at 15-minute intervals by the autosampler valve on the GC (1.2 mL volume sample of the gaseous products in the cell's headspace).

A Bruker 400 MHz nuclear magnetic resonance (NMR) spectrometer was used for one-dimensional ^{1}H NMR analysis with water suppression for CO_2RR liquid product analysis. The NMR samples were prepared using 500 µl of the analyte solution, 5 µm of a 10 mM DMSO solution and 10 µl D_2O. The concentration of liquid-phase CO_2RR products were determined by comparison to a DMSO standard added to the analyte before NMR analysis. The measurement of each product concentration was calculated using (Equation 2), where I is the intensity of the peak, N is number of peaks, M is the molar mass of the compound, W is the volumetric density

of each analyte, and P is the concentration. The subscripts "x" and "std" denote the analyte and the internal standard (DMSO), respectively.[30,31]

	$P_x = \frac{I_x}{I_{std}} \frac{N_{std}}{N_x} \frac{M_x}{M} \frac{W_{std}}{W_x} P_{std}$	Equation 2

The faradaic efficiency for each product was then calculated from the overall charged passed as measured by the potentiostat (Equation 3), where n is the number of moles of each product calculated through quantitative measurements, Z is the number of moles of electrons required per mole of product, F is the Faraday constant (96485.3 C mol^{-1}), and Q is the total charge passed in units of coulombs during each 15-minute interval.[32,33]

	$FE = \frac{n \times F \times Z}{Q}$	Equation 3

Results and Discussion

Structural characterization of AD and BD Cu foams

AD and BD Cu foams grown on a Ni substrate were used to study the crystalline structure and the morphology of the foams using XRD. The Ni substrate was necessary to ensure that the Bragg reflections for copper were isolated to the growth of the dendrites. The peaks at 43.2° and 50.3° corresponding to the (111) and (200) Cu Bragg reflections, respectively, were used to determine crystallite size based on the Debye-Scherrer equation (shown in Equation S1). The XRD peaks corresponding to the Ni substrate were observed at 44.8° and 52.2°, offering more than 1° of separation from the copper peaks and thus, not interfering with the peak shape analysis. Instrumental peak broadening was determined by studying the (220) peak of a single crystal Si wafer. The Si (220) peak at 46.9° was chosen based on its angular proximity to the Cu peaks of interest to define the instrumental broadening more accurately. (Figure S2) shows the Si (220) and its Gaussian fit to determine instrumental broadening. Each Cu foam sample was measured twice with 90° rotations between runs to remove potential bias from growth anisotropy in the plane of the substrate.

As seen in Figure 1, the XRD spectra of the deposited foams show the presence of copper. We also observed intense peaks corresponding to the Ni substrate, which indicates that the deposited Cu foams were thin relative to the penetration depth of the incident beam. We prepared foams with short electrodeposition times for XRD analysis to limit the measurements to the initial growth in the early stages of deposition to measure any anisotropy in the growth. The peak intensity, the full width at half max (FWHM), and integrated area under the curve for the (111) and (200) Cu Bragg reflections were calculated by fitting the peaks to a Gaussian line shape as shown in Figure 1. The instrumental broadening was subtracted from the peak widths to identify broadening related to the characteristic domain size of each deposition method using

Equation S2. The Debye-Scherrer crystallite sizes (Table 1) along the (111) and (200) orientations of the AD Cu foam were significantly larger (34.9 nm and 14.6 nm, respectively) than for the BD Cu foam (16.8nm and 8.4nm, respectively) for BD Cu. The AD Cu foam showed significantly higher growth anisotropy in the initial stages of dendrite formation than BD Cu measured in Figure 1. This can be measured from the ratio of the integrated intensities for the (111) and (200) Cu Bragg reflections. For reference, the ratio of integrated intensities A(111)/A(200) for an azimuthally-averaged Cu powder sample is 2.3.[34] The corresponding ratio for the BD Cu foam, A(111)/A(200) = 1.95, shows a slight anisotropy with respect to the surface normal. For the AD Cu foam, A(111)/A(200) = 1.02, which indicates that the growth direction preferentially oriented with respect to the electrode surface normal. This indicates that the dendritic growth in both solutions is likely to produce crystals that have preferred directions and are not randomly oriented. The summary of these findings is shown in Table 1.

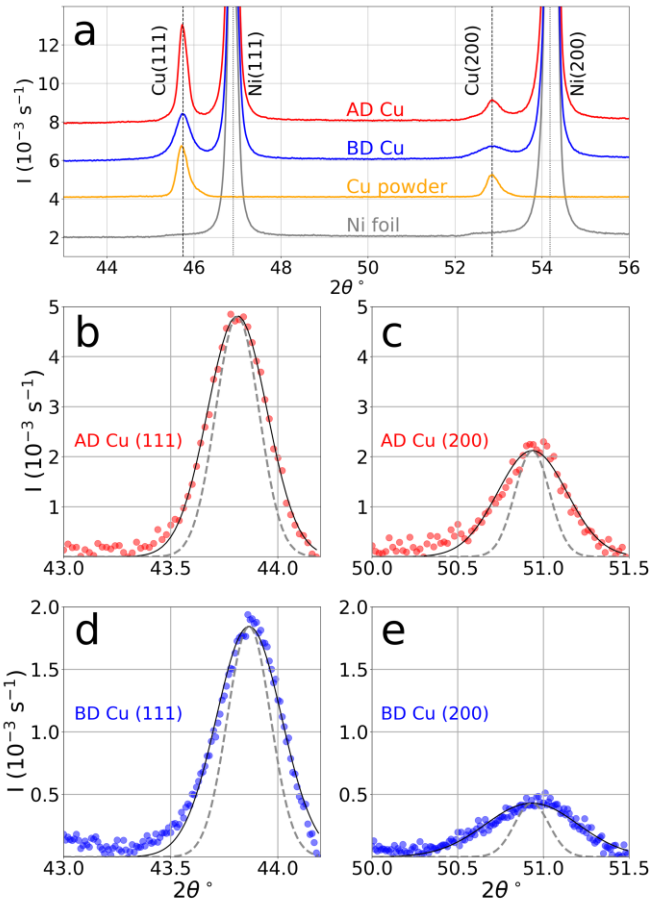

Figure 1: (a) 2θ XRD of acid and base deposited foams on nickel foil substrate, peaks corresponding to copper [111] and [200] planes seen at 43.6° and 50.8° in addition to copper powder and nickel foil. (b,c) Detailed view of AD Cu (111) and (200) XRD peaks. (d,e) Detailed view of BD Cu (111) and (200) XRD peaks. XRD data points (dots), instrumental broadening (gray dashed line), and gaussian fit (solid black line). Height ratio and broadening of the peaks can be attributed to growth orientation and crystalline size respectively.

Table 1: Crystallite size based on the (111) and (200) planes in AD Cu and BD Cu, and their areal ratios based on XRD analysis.

	[111] size(nm)	[200] size (nm)	A([111])/A([200]) areal ratio
AD Cu	34.9	14.6	1.02
BD Cu	16.8	8.4	1.95
Powder Avg Cu	-	-	2.3

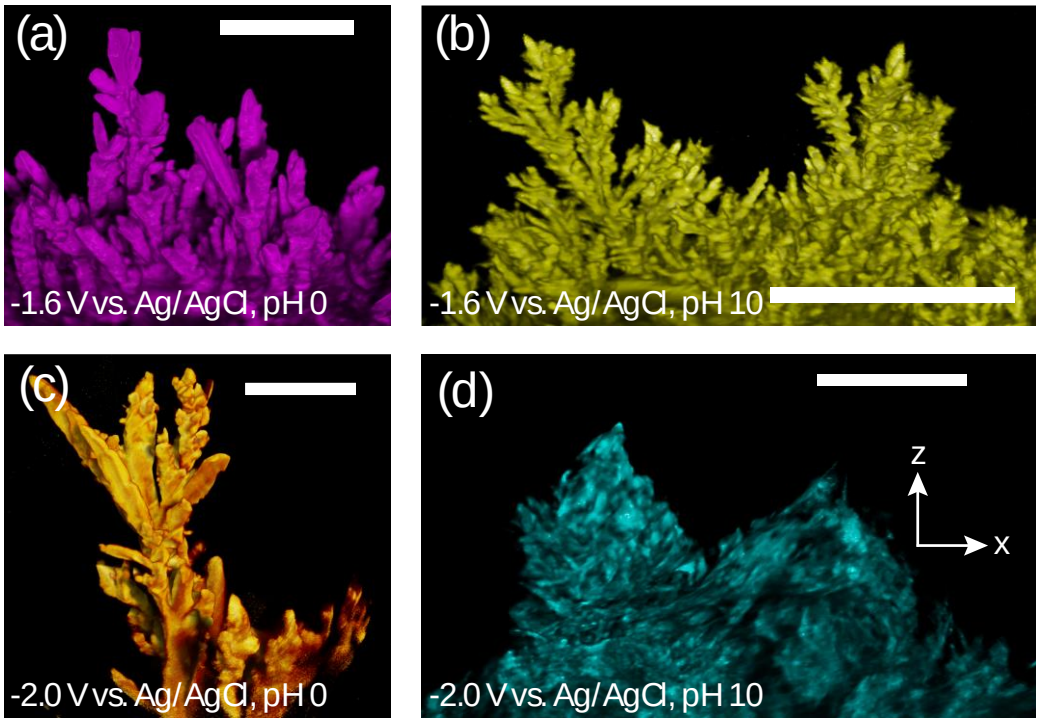

Figure 2 – NanoCT reconstructions of (a) AD Cu dendrites deposited at -1.6 V vs. Ag/AgCl, (b) BD dendrites deposited at -1.6 V vs. Ag/AgCl, (c) AD dendrites deposited at -2.0 V vs. Ag/AgCl, and (d) BD dendrites deposited at -2.0 V vs. Ag/AgCl. The scale bar in each figure represents 10 µm.

We characterized the nanoscale morphology of the AD and BD Cu dendrites using synchrotron-based nanoCT imaging (resolution ≈ 40-50 nm).[35] We used abbreviated depositions to limit the growth of each foam to the tip of a sharp sewing needle. The needle electrode facilitated the necessary rotation of the aligned sample to collect the rotated image sequence for the nanoCT process. At the lower deposition potential of -1.6 V vs. Ag/AgCl, the AD Cu dendrites (Figure 2a) showed growth generally along a single dimension with a small degree of branching. This was consistent with the observation of directional growth in AD Cu foam electrodes in XRD measurements. At the same potential, the BD Cu dendrites (Figure 2b) exhibited a smaller characteristic feature size and a higher degree of branching. At -2.0 V vs. Ag/AgCl, the AD Cu dendrites were slightly larger than at -1.6 V vs. Ag/AgCl (Figure 2c) but showed similar directed growth with limited branching. For comparison, the BD Cu dendrites deposited at -2.0 V vs. Ag/AgCl showed increased branching to the degree that the characteristic dimension of the structure is unresolvable in the nanoCT reconstruction. The nanostructure of these dendrites was consistent with the disparate characteristic grain size between the AD Cu and BD Cu dendrites from Debye-Scherrer analysis in Table 1.

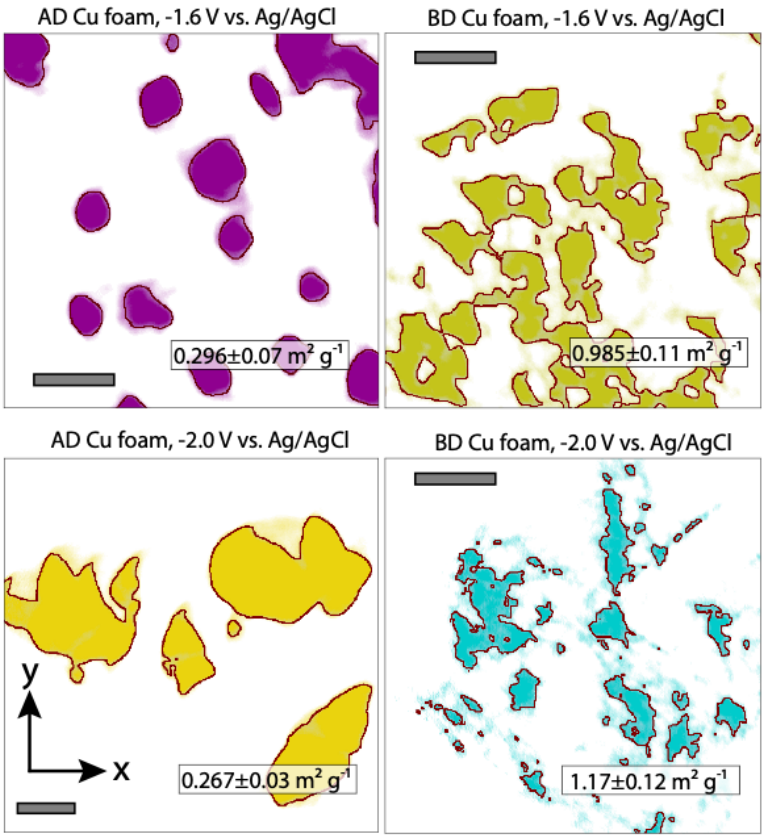

Figure 3 – Canny edge detection analysis of the perimeter of Cu dendrites in individual x-y slices of TXM reconstructions of AD Cu and BD Cu dendritic depositions. The Cu densities derived from the TXM tomograms are shown in purple. The corresponding Canny-determined perimeters are noted by the red line. The calculations of surface area-to-mass ratios are calculated from the mean values of the surface area and volume (mass density of Cu = 8.96 g cm^{-3}) for 400 consecutive slices through the TXM reconstructions (Figure 2), avoiding the regions including the pin electrode. The gray scale bar represents 2 µm in each slice.

The TXM reconstruction allowed us to measure important quantities such as the surface area and volume of the dendritic depositions. Given an x-y slice of the reconstruction, we computed

the edge profile of the Cu using the Canny edge-detection algorithm[36] implemented in scikit-image Python library.[37] The volume of Cu in the slice was calculated from the area of high density bounded by the Canny-detected perimeter times the thickness of the slice (dz = 18.7 ± 0.5 nm) in these reconstructions). Based on scanning electron microscopy analysis described below, we assume that the dendritic Cu is solid and has the same mass density as bulk copper (8.96 g cm^{-3}). Similarly, the surface area was computed from the length of the perimeter times the slice thickness. Examples of the edge detection for each TXM reconstruction are shown in (Figure 3). The Canny analysis showed that the surface area-to-mass ratio for AD Cu dendrites were 0.296 ± 0.07 m^2 g^{-1} and 0.267 ± 0.03 m^2 g^{-1} for the reconstructions of AD Cu dendrites grown at -1.6 V vs. Ag/AgCl and -2.0 V vs. Ag/AgCl, respectively. For the BD Cu dendrites, the surface area-to-mass ratio was 0.985 ± 0.11 m^2 g^{-1} for the sample grown at -1.6 V vs. Ag/AgCl and 1.17 ± 0.12 m^2 g^{-1} for the sample grown at -2.0 V vs. Ag/AgCl. The noted standard deviation is the variance of this ratio as calculated for each slice through the material. The Canny edge detection algorithm relies on a threshold value to differentiate the Cu from air. For the larger features in the AD Cu reconstructions, the edges are relatively well defined. For the smaller features of the BD Cu dendrites, the noise in the reconstruction makes edge detection somewhat ambiguous. This can lead to an undercounting of smaller, high surface area-to-mass ratio features that would result in an underestimation of the ratio measurements in BD Cu samples. The assumption that the area bounded by the Canny analysis edge sets an upper limit on the mass of a particular section through the slice. If pores are present that are smaller than the resolution limits of the instrument, then this would both increase the surface area and decrease the mass of the section. Regardless of this ambiguity, the Canny analysis shows that the electrodeposition conditions impart considerable experimental control over the structural and related functional properties of the deposited foam. An example relevant to electrocatalysis is

the ratio of the active area to the mass of a material, which is simply the surface area-to-volume ratio computed here scaled by the density of the Cu metal.

The copper foams on nickel substrates were studied using scanning electron microscopy (SEM). The AD Cu foams showed a multi-scale foam composed of dense structures of dendritic Cu between a network of larger voids templated by hydrogen bubbling with an average diameter of 78 ± 25 μm as seen in (Figure 4a). In comparison (Figure 4 b), the BD Cu foam formed a compact morphology with no apparent structural templating by hydrogen evolution during the growth. The bloom-like dendrites showed smaller particle sizes, and an isotropic growth (Figure 4d) compared to the directed, needle-like dendrites of the AD Cu foam (Figure 4c). The dendrites in both AD and BD Cu foams resembled the single dendrites observed in the TXM analysis, with more extensive branching due to prolonged deposition.

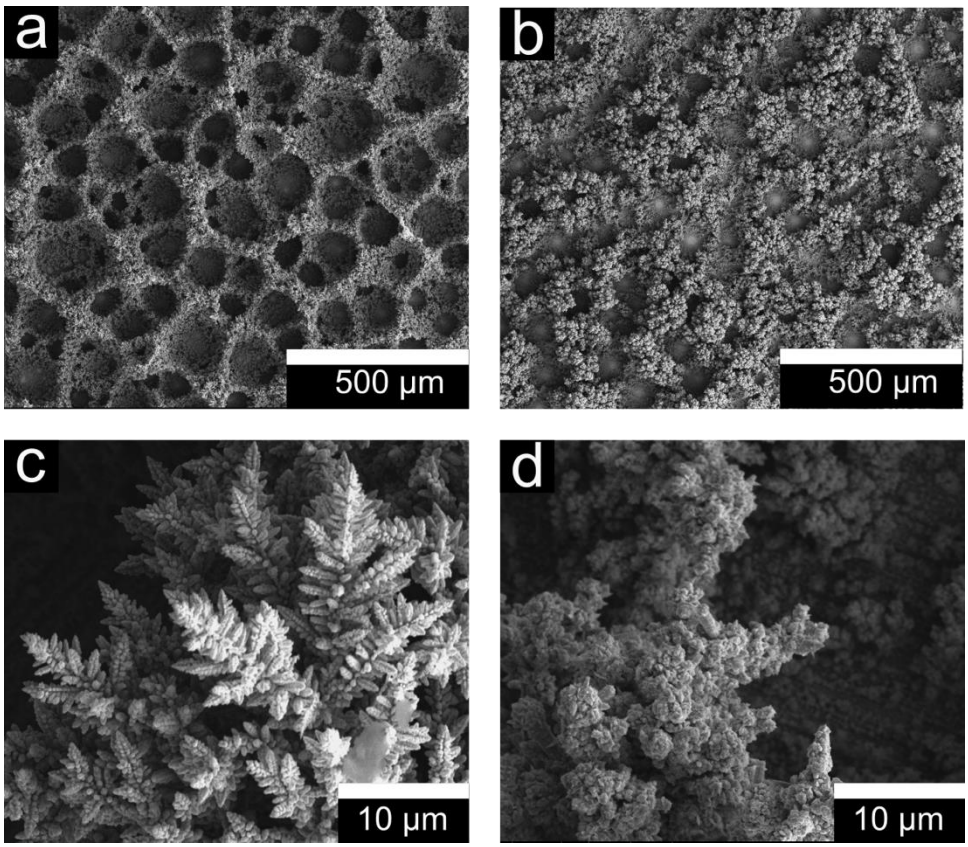

Figure 4: SEM images of an (a) AD Cu foam with DHBT foam structure. (b) BD Cu foam structure with minimal bubble induced void formation. (c) AD Cu dendrite closeup view with highly directional dendrite formation. (d) BD Cu dendrite in closeup view, with dendrites comprised of extremely small Cu crystallites as determined by XRD.

Electrocatalytic properties of AD and BD foam electrodes

As shown above, the structure and morphology of Cu foam electrodes can be controlled by the electrochemical environment during deposition. The surface morphology, in turn, can affect the functional properties of the deposited material. Cu foams are of particular interest to electrocatalysis due to the high electrochemically active surface area, simple fabrication, and

mechanical and electrochemical stability under high geometric current densities.[38] They can be used as current collectors for oxygen evolution reaction (OER) or HER electrocatalysts in water electrolysis. Both reactions involve the evolution of gas bubbles at even modest current densities. Surfaces with poor bubble nucleation properties can build up the local concentration of H_2, which generates a Nernstian shift of the thermodynamic reduction potential to more negative potentials. Promoting the formation and detachment of bubbles help to alleviate the local supersaturation of evolved products and their unfavorable effect on electrocatalysis.

We studied the bubble evolution properties of AD and BD Cu foams under identical galvanostatic conditions to compare the functional differences. Figure 5 shows cyclic voltammetry (CV) measurements of the electrodes in 0.2 M H_2SO_4 solution. AD Cu and BD Cu have similar onset potentials for HER (-10 mA cm^{-2} at -0.6 V vs. Ag/AgCl) and have similar current densities at more negative potentials. HER electrocatalysis on the AD Cu foam is practically indistinguishable from the BD Cu foam when considering the *j-E* behavior. However, H_2 bubble evolution plays a far more significant role in the morphology of the AD Cu foam electrodes than in the BD Cu foams. Bubble nucleation, therefore, may be favored on the AD Cu foam electrodes due to preexisting nucleation sites formed during DHBT.

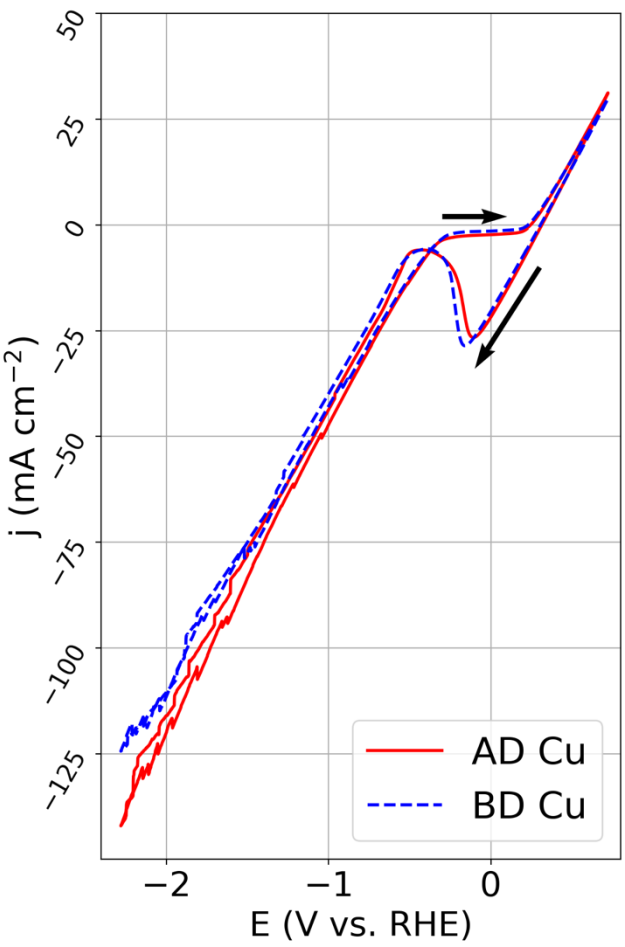

Figure 5: Cyclic voltammetry of AD Cu (solid red) and BD Cu (dashed blue) in 0.2 M H_2SO_4 between 0.5 V and -2.5 V vs. RHE. Fluctuations in plots at potentials more negative than -1.0 V vs Ag/AgCl was due to hydrogen bubbling as a result of HER.

We characterized H_2 bubble evolution, and detachment dynamics by imaging bubble evolution on AD and BD Cu foams at a fixed geometric current density (-5 mA cm^{-2}). This allowed for comparing the foam structures for their interactions with the growing bubbles at a constant rate of H_2 evolution. We characterized a total of 180 bubbles from their formation to their detachment

from the surface on each type of foam electrode. On average the HER bubbling site density was on average 42 mm^{-2} on the AD Cu foam and 19 mm^{-2} on the BD Cu foam as represented by yellow dots on the respective surfaces of foam electrodes in Figures 6c and 6d. Notably, the areal rate of bubbling on AD Cu was 20.1 events mm^{-2} s^{-1}, whereas, for BD Cu, this rate was 1.8 mm^{-2} s^{-1}. Considering that the rate of hydrogen evolution on both electrodes is similar, it can be inferred that the dissolved hydrogen in the solution near the BD Cu electrode must be higher than that of AD Cu electrode. As shown in Figure 6a, the dwell time (average time in seconds where a bubble is attached to the surface from formation to detachment) of the hydrogen bubbles on the AD Cu was 0.58 s, compared to the BD Cu with a mean dwell time of 0.35 s. The bubbles leaving the BD Cu foam were also larger on average at the time of detachment (26 $\pm$ 6 µm) than those leaving the AD Cu foam (21 $\pm$ 5 µm). A t-test analysis confirming statistical differences of the bubble size distribution is provided in the Supporting Information. Hence, bubbles appear significantly less frequently on the surface, then grow and detach more rapidly from the BD Cu foam electrode than the AD Cu one at the same H_2 evolution rate. Based on the measured average diameters, the average bubble volume for the BD Cu foam is roughly 90% larger (9200 μm^3) than for the AD Cu foam (4900 μm^3). Nevertheless, this volume increase per bubble does not mitigate the more than 11-fold decrease in bubbling rate obcerved on the BD Cu foam. The faster growth rate of bubbles on the BD Cu foam suggests that the local concentration of H_2 near the surface of BD Cu foam is higher than that of AD Cu foam. This follows from models for the time dependent radius of a bubble, R(t), as a function of the difference between the concentration of the dissolved gas in the near-electrode bulk electrolyte (c_b) and the concentration of dissolved gas at the gas-electrolyte interface (c_i):[39,40]

	$R(t) \propto t\sqrt{(c_b - c_i)}$	Equation 5

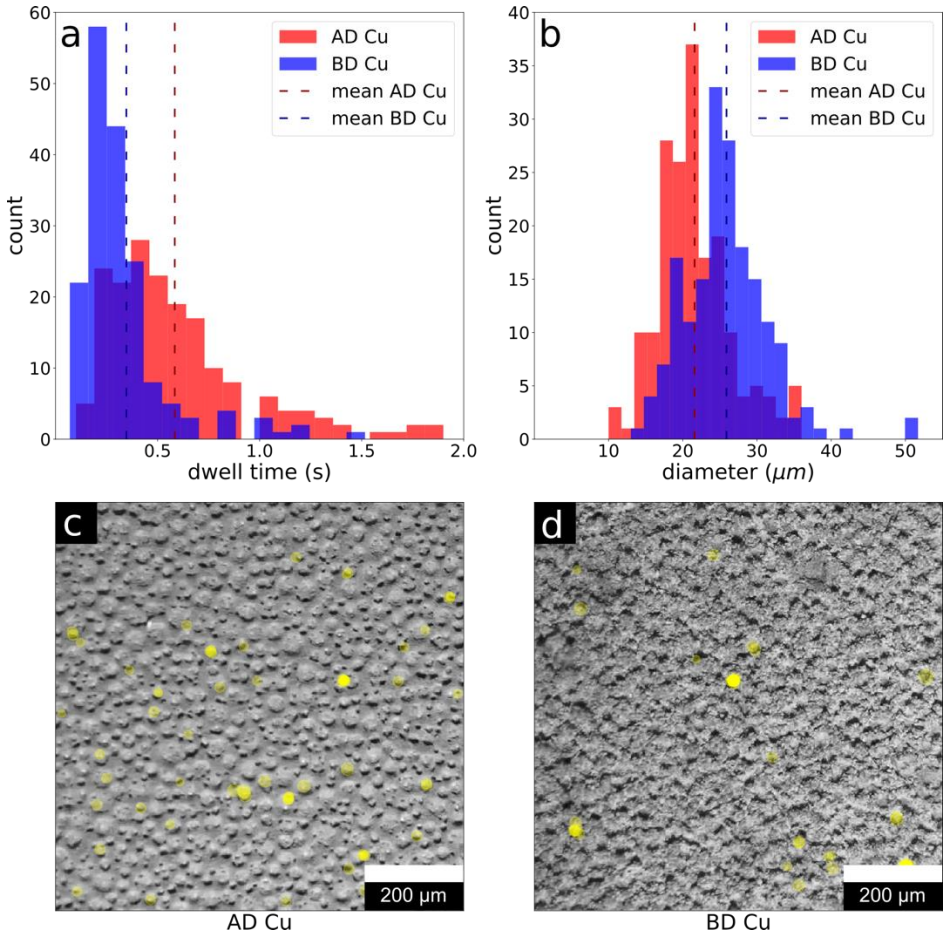

Figure 6: (a) The distribution of dwell times during HER on AD Cu and BD Cu foams. (b) The bubble diameter distribution during HER on AD Cu and BD Cu at -2.0V vs. Ag/AgCl. (c) acid deposited and (d) base deposited copper foam before HER with the bubble location shown in yellow. The size of each yellow circle corresponds with the bubble diameter at the time of separation.

Cu foams are interesting substrates for electrocatalysis in their own right. Metallic copper has been studied as a CO_2 reduction reaction (CO_2RR) electrocatalyst due to its wide array of products ranging from simple hydrocarbons such as methane, ethane, and ethylene to oxygenates such as alcohols, aldehydes, and ketones.[32,41–43] Simulation studies have proposed mechanisms for the catalytic conversion of CO_2 to C_{2+} products. These mechanisms are

generally complex, multistep processes with some steps involving desorption and re-adsorption of the surface absorbed intermediate products.[44,45] The frequency of these re-adsorption events can potentially be improved by increasing the tortuosity of the structure of the electrocatalyst to prevent the diffusion to the bulk electrolyte. Dendritic copper foams are therefore advantageous structures for C_{2+} production from CO_2 reduction.[46–48]

We studied how the different Cu foam structures can influence CO_2RR catalysis. Figure 8 shows the faradaic efficiency (FE) of the gaseous CO_2 reduction products detected in the headspace of the cathode compartment. At -0.8 V vs. RHE, AD Cu and BD Cu produce H_2, CO, C_2H_4, and C_2H_6. The faradaic share of hydrogen reduction shows an increasing trend from -0.8 V vs. RHE to -1.2V vs. RHE, starting at 51.7% reaching over 62.1% for AD Cu and from 36.4% to 50.5% for BD Cu. CO production was maximum at -0.8 V vs. RHE for both copper morphologies and decreased to less than 1% at -1.2 V vs. RHE. The overall rates of CO production were low compared to planar, polycrystalline Cu electrocatalysts.[32] Ethylene and ethane were the main gas-phase CO_2RR product on both copper foam morphologies. The highest amount of faradaic efficiency towards ethane was seen at -0.8 V vs. RHE at 15.7% and 17.2% in AD Cu and BD Cu, respectively. More negative potentials show lower ethane. At -1.2 V vs. RHE, the faradaic efficiency drops to less than 8.9% for both AD Cu and BD Cu. Ethylene showed the opposite trend with potential; at -0.8 V vs. RHE, the Faradaic efficiency of this product for AD Cu and BD Cu were 1.3% and 0%. These yields increased to 5.1% and 1.4% for AD Cu and BD Cu at -1.2 V vs. RHE. The ratio of ethane to ethylene in AD Cu at -0.8 V vs. RHE was 13 and decreased to 2 at more negative potentials. This trend was also seen in BD Cu, where this ratio is near infinity (ethylene is not detected) at –0.8 V vs. RHE and decreases to 6 at –1.2 V vs. RHE. At each potential, the BD Cu electrocatalyst is especially selective to ethane

production compared to other gas phase CO_2RR products. A detailed table of the product's average faradaic efficiencies and their standard deviations can be found in Table S1.

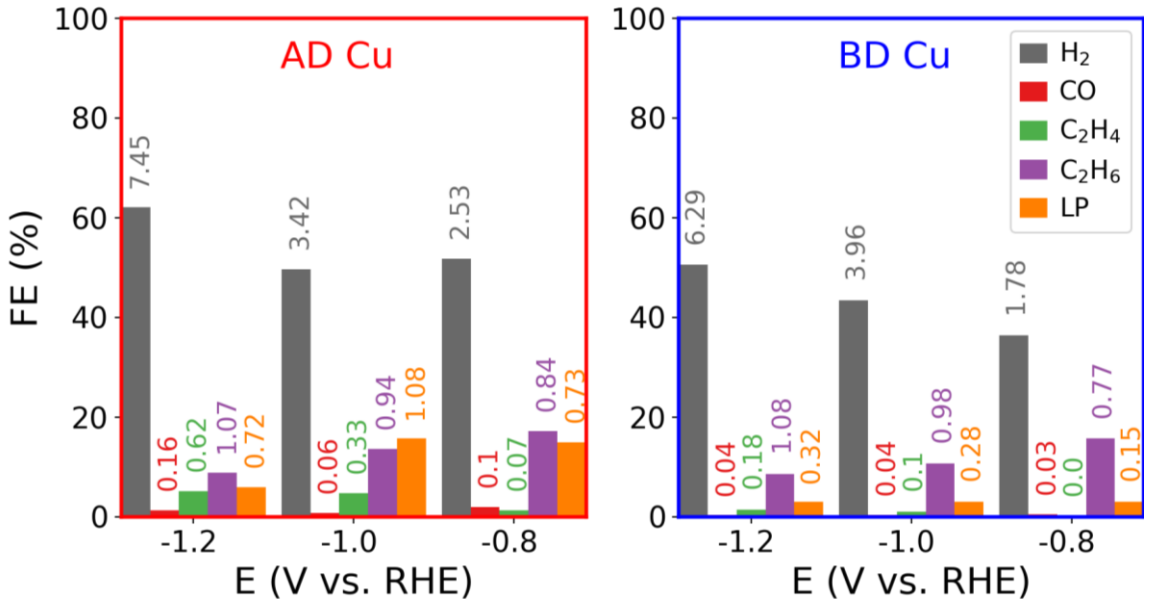

Figure 8: Average faradaic efficiency and partial cathodic current densities (in mA cm^{-2}) of H_2, CH_4, C_2H_4, C_2H_6, and liquid products (LP) of left) AD Cu and, right) BD Cu at CO_2RR at -1.2, -1.0, -0.8 V vs. RHE.

^{1}H NMR analysis of the electrolyte from the cathode compartment (Figure S5) showed that both Cu foams produced a range of C_1 and C_2 products, including formate, ethanol, and acetate. Lactic acid was observed only in the BD Cu foams, though this is attributed to the remaining contamination from the electrodeposition process of these foams. We observed that the AD Cu foams produced up to 15% faradaic efficiency towards liquid products (at -1.0 V vs. RHE), whereas the BD Cu foams had liquid products FEs of 3% regardless of CO_2RR potential. The partial current densities (*j*) of each product can be seen on top of each bar in Figure 8. For all products, the partial current density showed an increasing trend with more negative potentials for each foam electrocatalyst. The partial current density for C_2H_6 was only a function of

potential and independent of the catalyst morphology. The most significant liquid product for both foam electrocatalysts was formate which was seen in all samples with FEs near 3-4%. In addition, 1-propanol and ethanol were detected as CO_2RR products of AD Cu foam electrocatalysts. Standard liquid-phase CO_2RR products, such as methanol, acetone, and acetate, were not observed in the ^{1}H NMR analysis of the electrolyte. The detailed table of faradaic efficiencies of all gaseous and liquid products can be found in the SI.

Low faradaic efficiencies toward CO and no detectable amount of methane produced by either Cu foam electrocatalyst suggest the structure is capable of suppressing C_1 product mechanisms, as has been reported previously.[49–52] One possible explanation is that CO can be reabsorbed to the electrode surface and undergo further reduction reaction, which becomes more likely in a tortuous structure where the possibility of multiple interactions with the electrocatalyst surface is high. Methane production requires an adsorbed *CO species to go through four hydrogenation reactions without creating C-C dimerization. One potential explanation for this shift in products is that the energetics of the electrocatalyst surface facilitates C-C coupling in adsorbed *CO species. This pathway has been reported to be the thermodynamically preferred reaction on (100) copper facets.[41,53] In addition, the concentration of hydronium in the confined volume of the foam electrocatalysts is lower than that of the bulk solution, improving the kinetics of C-C bond formation.[14,54] Methane formation is also a pH-dependent process and is less likely within the internal structure of foam electrocatalysts.[3,52] Studies have shown that the pH at the working electrode, the local pH can increase nearly three pH units from the bulk pH of 6.8 due to local hydroxide ion formation during HER and CO_2RR.[12,14,55–57] Equation (6) shows the stoichiometrically balanced reaction of CO_2 to C_2H_6 where 12 mole equivalents of H^+ are consumed in the reduction reaction.

	$2CO_2 + 12H^+ + 12e^- \rightarrow 2C_2H_6 + 4H_2O$	Equation 6

A secondary effect of depletion of protons within the interior of the electrode during CO_2RR and HER is the Nernstian shift of the proton reduction potential, seen in Equation (7). While the dissolved hydrogen in the bulk solution reaches an equilibrium with the gas phase and remains constant throughout the reaction, the tortious structure of the electrode can limit the diffusion of H_2 from the interior of the electrode to the bulk solution, as observed in the HER electrolysis experiments here. As a result, the electrochemical potential for HER shifts towards more negative potentials. Considering overpotentials associated with hydrogen evolution, we can predict that HER is suppressed within the electrode volume in terms of reaction thermodynamics. This effect should be more pronounced in the base deposited copper foams which lack the hydrogen bubbling voids observed in acid deposited foams. The experimental evidence here shows that AD Cu electrocatalysts resulted in a higher faradaic efficiency and partial current density for H_2 than BD Cu at each potential measured.

	$E_{(H_2/H^+)} = E^0_{(H_2/H^+)} - \frac{RT}{nf}\log\frac{[H_2]}{[H^+]}$	Equation 7

Conclusions

Based on the results presented, we conclude that the composition of the deposition solution plays a crucial role in determining the morphology, microstructure, and electrocatalytic function of dendritic Cu foam electrodes. The pH and effect of the stabilizing ligands on Cu^{2+}(aq) ions in the deposition solution affects the crystallite size distribution and preferred growth direction. SEM and nanoCT imaging show that the size and shape of the copper crystals in addition to dynamic hydrogen bubble templating are also affected by the availability of protons in the

solution. These structural differences, in turn, are important factors in the catalytic activity of the dendritic copper foams. BD Cu showed lower faradaic yields towards H_2 and higher ethane specificity compared to AD Cu. We hypothesize that the efficacy of copper foams as an electrocatalyst for water splitting can be affected by the deposition conditions. Namely, the DHBT process that occurs in acidic electrolyte can potentially create more favorable conditions for hydrogen evolution during CO_2RR. The effects of pH on dendritic deposition can be observed from nanometer to millimeter length scales and can be tuned to fabricate copper dendrites with optimized properties for specific applications.

Acknowledgements

We acknowledge the Alfred P. Sloan Foundation under Grant Number G-2021-12156 and the University of Arkansas Chancellor's Innovation and Collaboration Fund for supporting this research. Use of the Stanford Synchrotron Radiation Lightsource, SLAC National Accelerator Laboratory, is supported by the U.S. Department of Energy, Office of Science, Office of Basic Energy Sciences under Contract No. DE-AC02-76SF00515. We also thank Dr. Zebulon Schichtl, Dr. James A. Lowe, and Dr. Mourad Benamara for helpful discussions.

References

(1) Wang, S.; Guan, B. Y.; Lu, Y.; Lou, X. W. "David." Formation of Hierarchical In_2S_3–$CdIn_2S_4$ Heterostructured Nanotubes for Efficient and Stable Visible Light CO_2 Reduction. *J. Am. Chem. Soc.* **2017**, *139* (48), 17305–17308. https://doi.org/10.1021/jacs.7b10733.

(2) Yang, H.; Hao, X.; Tang, J.; Jin, W.; Liu, C.; Hou, H.; Ji, X.; Hu, J. Dual-Functional Porous Copper Films Modulated via Dynamic Hydrogen Bubble Template for in Situ SERS Monitoring Electrocatalytic Reaction. *Appl. Surf. Sci.* **2019**, *494*, 731–739. https://doi.org/10.1016/j.apsusc.2019.07.241.

(3) Wang, S.; Wang, Y.; Zang, S.-Q.; Lou, X. W. (David). Hierarchical Hollow Heterostructures for Photocatalytic CO_2 Reduction and Water Splitting. *Small Methods* **2020**, *4* (1), 1900586. https://doi.org/10.1002/smtd.201900586.

(4) Tippets, C. A.; Fu, Y.; Jackson, A.-M.; Donev, E. U.; Lopez, R. Reproduction and Optical Analysis of Morpho-Inspired Polymeric Nanostructures. *J. Opt.* **2016**, *18* (6), 065105. https://doi.org/10.1088/2040-8978/18/6/065105.

(5) Argyros, A.; Manos, S.; Large, M. C. J.; McKenzie, D. R.; Cox, G. C.; Dwarte, D. M. Electron Tomography and Computer Visualisation of a Three-Dimensional `photonic' Crystal in a Butterfly Wing-Scale. **2002**, 5.

(6) Biró, L. P.; Bálint, Zs.; Kertész, K.; Vértesy, Z.; Márk, G. I.; Horváth, Z. E.; Balázs, J.; Méhn, D.; Kiricsi, I.; Lousse, V.; Vigneron, J.-P. Role of Photonic-Crystal-Type Structures in the Thermal Regulation of a Lycaenid Butterfly Sister Species Pair. *Phys. Rev. E* **2003**, *67* (2), 021907. https://doi.org/10.1103/PhysRevE.67.021907.

(7) Fu, Y.; Tippets, C. A.; Donev, E. U.; Lopez, R. Structural Colors: From Natural to Artificial Systems. *WIREs Nanomedicine Nanobiotechnology* **2016**, *8* (5), 758–775. https://doi.org/10.1002/wnan.1396.

(8) Wen, C.; Guo, H.; Bai, H.; Xu, T.; Liu, M.; Yang, J.; Zhu, Y.; Zhao, W.; Zhang, J.; Cao, M.; Zhang, L. Beetle-Inspired Hierarchical Antibacterial Interface for Reliable Fog Harvesting. *ACS Appl. Mater. Interfaces* **2019**, *11* (37), 34330–34337. https://doi.org/10.1021/acsami.9b11862.

(9) Wang, L.; Nitopi, S.; Wong, A. B.; Snider, J. L.; Nielander, A. C.; Morales-Guio, C. G.; Orazov, M.; Higgins, D. C.; Hahn, C.; Jaramillo, T. F. Electrochemically Converting Carbon Monoxide to Liquid Fuels by Directing Selectivity with Electrode Surface Area. *Nat. Catal.* **2019**, *2* (8), 702–708. https://doi.org/10.1038/s41929-019-0301-z.

(10) Braga, A. H.; Costa, N. J. S.; Philippot, K.; Gonçalves, R. V.; Szanyi, J.; Rossi, L. M. Structure and Activity of Supported Bimetallic NiPd Nanoparticles: Influence of Preparation Method on CO_2 Reduction. *ChemCatChem* **2020**, *12* (11), 2967–2976. https://doi.org/10.1002/cctc.201902329.

(11) Laskowski, F. A. L.; Oener, S. Z.; Nellist, M. R.; Gordon, A. M.; Bain, D. C.; Fehrs, J. L.; Boettcher, S. W. Nanoscale Semiconductor/Catalyst Interfaces in Photoelectrochemistry. *Nat. Mater.* **2020**, *19* (1), 69–76. https://doi.org/10.1038/s41563-019-0488-z.

(12) Hall, A. S.; Yoon, Y.; Wuttig, A.; Surendranath, Y. Mesostructure-Induced Selectivity in CO_2 Reduction Catalysis. *J. Am. Chem. Soc.* **2015**, *137* (47), 14834–14837. https://doi.org/10.1021/jacs.5b08259.

(13) Wang, L.; Nitopi, S. A.; Bertheussen, E.; Orazov, M.; Morales-Guio, C. G.; Liu, X.; Higgins, D. C.; Chan, K.; Nørskov, J. K.; Hahn, C.; Jaramillo, T. F. Electrochemical Carbon Monoxide Reduction on Polycrystalline Copper: Effects of Potential, Pressure, and PH on Selectivity toward Multicarbon and Oxygenated Products. *ACS Catal.* **2018**, *8* (8), 7445–7454. https://doi.org/10.1021/acscatal.8b01200.

(14) Klingan, K.; Kottakkat, T.; Jovanov, Z. P.; Jiang, S.; Pasquini, C.; Scholten, F.; Kubella, P.; Bergmann, A.; Roldan Cuenya, B.; Roth, C.; Dau, H. Reactivity Determinants in Electrodeposited Cu Foams for Electrochemical CO_2 Reduction. *ChemSusChem* **2018**, *11* (19), 3449–3459. https://doi.org/10.1002/cssc.201801582.
(15) Matsushita, M.; Honda, K.; Toyoki, H.; Hayakawa, Y.; Kondo, H. Generalization and the Fractal Dimensionality of Diffusion-Limited Aggregation. *J. Phys. Soc. Jpn.* **1986**, *55* (8), 2618–2626. https://doi.org/10.1143/JPSJ.55.2618.
(16) Cogswell, D. A. Quantitative Phase-Field Modeling of Dendritic Electrodeposition. *Phys. Rev. E* **2015**, *92* (1), 011301. https://doi.org/10.1103/PhysRevE.92.011301.
(17) Beverskog, B.; Puigdomenech, I. Revised Pourbaix Diagrams for Copper at 25 to 300°C. *J. Electrochem. Soc.* **1997**, *144* (10), 3476–3483. https://doi.org/10.1149/1.1838036.
(18) Li, Y.; Jia, W.-Z.; Song, Y.-Y.; Xia, X.-H. Superhydrophobicity of 3D Porous Copper Films Prepared Using the Hydrogen Bubble Dynamic Template. *Chem. Mater.* **2007**, *19* (23), 5758–5764. https://doi.org/10.1021/cm071738j.
(19) Yao, X.; Xu, L.; Jiang, L. Fabrication and Characterization of Superhydrophobic Surfaces with Dynamic Stability. *Adv. Funct. Mater.* **2010**, *20* (19), 3343–3349. https://doi.org/10.1002/adfm.201000013.
(20) Plowman, B. J.; Jones, L. A.; Bhargava, S. K. Building with Bubbles: The Formation of High Surface Area Honeycomb-like Films via Hydrogen Bubble Templated Electrodeposition. *Chem. Commun.* **2015**, *51* (21), 4331–4346. https://doi.org/10.1039/C4CC06638C.
(21) Bard, A. J.; Faulkner, L. R. *Electrochemical Methods: Fundamentals and Applications*, 2nd ed.; Wiley: New York, 2001.
(22) Achilli, E.; Vertova, A.; Visibile, A.; Locatelli, C.; Minguzzi, A.; Rondinini, S.; Ghigna, P. Structure and Stability of a Copper(II) Lactate Complex in Alkaline Solution: A Case Study by Energy-Dispersive X-Ray Absorption Spectroscopy. *Inorg. Chem.* **2017**, *56* (12), 6982–6989. https://doi.org/10.1021/acs.inorgchem.7b00553.
(23) Golden, T. D.; Shumsky, M. G.; Zhou, Y.; VanderWerf, R. A.; Van Leeuwen, R. A.; Switzer, J. A. Electrochemical Deposition of Copper(I) Oxide Films. *Chem. Mater.* **1996**, *8* (10), 2499–2504. https://doi.org/10.1021/cm9602095.
(24) de Jongh, P. E.; Vanmaekelbergh, D.; Kelly, J. J. Cu_2O: Electrodeposition and Characterization. *Chem. Mater.* **1999**, *11* (12), 3512–3517. https://doi.org/10.1021/cm991054e.
(25) Paracchino, A.; Laporte, V.; Sivula, K.; Grätzel, M.; Thimsen, E. Highly Active Oxide Photocathode for Photoelectrochemical Water Reduction. *Nat. Mater.* **2011**, *10* (6), 456–461. https://doi.org/10.1038/nmat3017.
(26) Lowe, J.; Coridan, R. H. Mechanistic Control of a Galvanic Replacement Reaction on Cuprous Oxide. *Nanoscale Adv.* **2019**, *1* (4), 1343–1350. https://doi.org/10.1039/C8NA00396C.
(27) Liu, Y.; Meirer, F.; Williams, P. A.; Wang, J.; Andrews, J. C.; Pianetta, P. *TXM-Wizard* : A Program for Advanced Data Collection and Evaluation in Full-Field Transmission X-Ray Microscopy. *J. Synchrotron Radiat.* **2012**, *19* (2), 281–287. https://doi.org/10.1107/S0909049511049144.
(28) Bradski, G. The OpenCV Library. *Dr Dobbs J. Softw. Tools Prof. Program.* **2000**, *25* (11).
(29) Schneider, C. A.; Rasband, W. S.; Eliceiri, K. W. NIH Image to ImageJ: 25 Years of Image Analysis. *Nat. Methods* **2012**, *9* (7), 671–675. https://doi.org/10.1038/nmeth.2089.
(30) Pauli, G. F.; Gödecke, T.; Jaki, B. U.; Lankin, D. C. Quantitative ^{1}H NMR. Development and Potential of an Analytical Method: An Update. *J. Nat. Prod.* **2012**, *75* (4), 834–851. https://doi.org/10.1021/np200993k.

(31) Malz, F.; Jancke, H. Validation of Quantitative NMR. *J. Pharm. Biomed. Anal.* **2005**, *38* (5), 813–823. https://doi.org/10.1016/j.jpba.2005.01.043.
(32) Kuhl, K. P.; Cave, E. R.; Abram, D. N.; Jaramillo, T. F. New Insights into the Electrochemical Reduction of Carbon Dioxide on Metallic Copper Surfaces. *Energy Environ. Sci.* **2012**, *5* (5), 7050. https://doi.org/10.1039/c2ee21234j.
(33) Aitchison, C. M.; Andrei, V.; Antón-García, D.; Apfel, U.-P.; Badiani, V.; Beller, M.; Bocarsly, A. B.; Bonnet, S.; Brueggeller, P.; Caputo, C. A.; Cassiola, F.; Clausing, S. T.; Cooper, A. I.; Creissen, C. E.; de la Peña O'Shea, V. A.; Domcke, W.; Durrant, J. R.; Grätzel, M.; Hammarström, L.; Hankin, A.; Hatzell, M. C.; Karadas, F.; König, B.; Kuehnel, M. F.; Lamaison, S.; Lin, C.-Y.; Maneiro, M.; Minteer, S. D.; R. Paris, A.; Pastor, E.; Pornrungroj, C.; Reek, J. N. H.; Reisner, E.; Roy, S.; Sahm, C.; Shankar, R.; Shaw, W. J.; Shylin, S. I.; Smith, W. A.; Sokol, K.; Soo, H. S.; Sprick, R. S.; Viertl, W.; Vogel, A.; Wagner, A.; Wakerley, D.; Wang, Q.; Wielend, D.; Zwijnenburg, M. A. Synthetic Approaches to Artificial Photosynthesis: General Discussion. *Faraday Discuss.* **2019**, 10.1039.C9FD90024A. https://doi.org/10.1039/C9FD90024A.
(34) Gates-Rector, S.; Blanton, T. The Powder Diffraction File: A Quality Materials Characterization Database. *Powder Diffr.* **2019**, *34* (4), 352–360. https://doi.org/10.1017/S0885715619000812.
(35) Andrews, J. C.; Brennan, S.; Pianetta, P.; Ishii, H.; Gelb, J.; Feser, M.; Rudati, J.; Tkachuk, A.; Yun, W. Full-Field Transmission x-Ray Microscopy at SSRL. *J. Phys. Conf. Ser.* **2009**, *186*, 012002. https://doi.org/10.1088/1742-6596/186/1/012002.
(36) Canny, J. A Computational Approach to Edge Detection. *IEEE Trans. Pattern Anal. Mach. Intell.* **1986**, *PAMI-8* (6), 679–698. https://doi.org/10.1109/TPAMI.1986.4767851.
(37) van der Walt, S.; Schönberger, J. L.; Nunez-Iglesias, J.; Boulogne, F.; Warner, J. D.; Yager, N.; Gouillart, E.; Yu, T. Scikit-Image: Image Processing in Python. *PeerJ* **2014**, *2*, e453. https://doi.org/10.7717/peerj.453.
(38) Sun, H.; Kim, H.; Song, S.; Jung, W. Copper Foam-Derived Electrodes as Efficient Electrocatalysts for Conventional and Hybrid Water Electrolysis. *Mater. Rep. Energy* **2022**, *2* (2), 100092. https://doi.org/10.1016/j.matre.2022.100092.
(39) Glas, J. P.; Westwater, J. W. Measurements of the Growth of Electrolytic Bubbles. *Int. J. Heat Mass Transf.* **1964**, *7* (12), 1427–1443. https://doi.org/10.1016/0017-9310(64)90130-9.
(40) Jones, S. F.; Evans, G. M.; Galvin, K. P. The Cycle of Bubble Production from a Gas Cavity in a Supersaturated Solution. *Adv. Colloid Interface Sci.* **1999**, *80* (1), 51–84. https://doi.org/10.1016/S0001-8686(98)00075-X.
(41) Hori, Y. Electrochemical CO_2 Reduction on Metal Electrodes. In *Modern aspects of electrochemistry*; Springer, 2008; pp 89–189.
(42) Clark, E. L.; Hahn, C.; Jaramillo, T. F.; Bell, A. T. Electrochemical CO_2 Reduction over Compressively Strained CuAg Surface Alloys with Enhanced Multi-Carbon Oxygenate Selectivity. *J. Am. Chem. Soc.* **2017**, *139* (44), 15848–15857. https://doi.org/10.1021/jacs.7b08607.
(43) DuChene, J. S.; Tagliabue, G.; Welch, A. J.; Cheng, W.-H.; Atwater, H. A. Hot Hole Collection and Photoelectrochemical CO_2 Reduction with Plasmonic Au/p-GaN Photocathodes. *Nano Lett.* **2018**, *18* (4), 2545–2550. https://doi.org/10.1021/acs.nanolett.8b00241.
(44) Montoya, J. H.; Peterson, A. A.; Nørskov, J. K. Insights into C-C Coupling in CO_2 Electroreduction on Copper Electrodes. *ChemCatChem* **2013**, *5* (3), 737–742. https://doi.org/10.1002/cctc.201200564.
(45) Montoya, J. H.; Shi, C.; Chan, K.; Nørskov, J. K. Theoretical Insights into a CO Dimerization Mechanism in CO_2 Electroreduction. *J. Phys. Chem. Lett.* **2015**, *6* (11), 2032–2037. https://doi.org/10.1021/acs.jpclett.5b00722.

(46) Gonçalves, M. R.; Gomes, A.; Condeço, J.; Fernandes, T. R. C.; Pardal, T.; Sequeira, C. A. C.; Branco, J. B. Electrochemical Conversion of CO_2 to C_2 Hydrocarbons Using Different Ex Situ Copper Electrodeposits. *Electrochimica Acta* **2013**, *102*, 388–392. https://doi.org/10.1016/j.electacta.2013.04.015.
(47) Sen, S.; Liu, D.; Palmore, G. T. R. Electrochemical Reduction of CO_2 at Copper Nanofoams. *ACS Catal.* **2014**, *4* (9), 3091–3095. https://doi.org/10.1021/cs500522g.
(48) Ahn, S. T.; Abu-Baker, I.; Palmore, G. T. R. Electroreduction of CO_2 on Polycrystalline Copper: Effect of Temperature on Product Selectivity. *Catal. Today* **2017**, *288*, 24–29. https://doi.org/10.1016/j.cattod.2016.09.028.
(49) Rashid, N.; Bhat, M. A.; Ingole, P. P. Dendritic Copper Microstructured Electrodeposits for Efficient and Selective Electrochemical Reduction of Carbon Dioxide into C1 and C2 Hydrocarbons. *J. COsub2sub Util.* **2020**, *38*, 385–397. https://doi.org/10.1016/j.jcou.2020.02.017.
(50) Zhang, W.; Huang, C.; Xiao, Q.; Yu, L.; Shuai, L.; An, P.; Zhang, J.; Qiu, M.; Ren, Z.; Yu, Y. Atypical Oxygen-Bearing Copper Boosts Ethylene Selectivity toward Electrocatalytic CO_2 Reduction. *J. Am. Chem. Soc.* **2020**, *142* (26), 11417–11427. https://doi.org/10.1021/jacs.0c01562.
(51) Karapinar, D.; Creissen, C. E.; Rivera de la Cruz, J. G.; Schreiber, M. W.; Fontecave, M. Electrochemical CO_2 Reduction to Ethanol with Copper-Based Catalysts. *ACS Energy Lett.* **2021**, *6* (2), 694–706. https://doi.org/10.1021/acsenergylett.0c02610.
(52) Xiang, K.; Liu, Y.; Li, C.; Liu, X.; Yi, H.; Wu, L.; Shen, F.; Liu, M.; Wang, P.; Liu, H. Microenvironmental Feeding and Stabilization of C_2H_4 Intermediates by Iodide-Doped Copper Nanowire Arrays to Boost C_2H_6 Formation. *Energy Fuels* **2021**, *35* (19), 15987–15994. https://doi.org/10.1021/acs.energyfuels.1c02616.
(53) Kortlever, R.; Shen, J.; Schouten, K. J. P.; Calle-Vallejo, F.; Koper, M. T. M. Catalysts and Reaction Pathways for the Electrochemical Reduction of Carbon Dioxide. *J Phys Chem Lett* **2015**, 10.
(54) Zheng, Y.; Vasileff, A.; Zhou, X.; Jiao, Y.; Jaroniec, M.; Qiao, S.-Z. Understanding the Roadmap for Electrochemical Reduction of CO_2 to Multi-Carbon Oxygenates and Hydrocarbons on Copper-Based Catalysts. *J. Am. Chem. Soc.* **2019**, *141* (19), 7646–7659. https://doi.org/10.1021/jacs.9b02124.
(55) Gupta, N.; Gattrell, M.; MacDougall, B. Calculation for the Cathode Surface Concentrations in the Electrochemical Reduction of CO_2 in $KHCO_3$ Solutions. *J. Appl. Electrochem.* **2006**, *36* (2), 161–172. https://doi.org/10.1007/s10800-005-9058-y.
(56) Wagner, A.; Sahm, C. D.; Reisner, E. Towards Molecular Understanding of Local Chemical Environment Effects in Electro- and Photocatalytic CO_2 Reduction. *Nat. Catal.* **2020**, *3* (10), 775–786. https://doi.org/10.1038/s41929-020-00512-x.
(57) Zhang, Z.; Melo, L.; Jansonius, R. P.; Habibzadeh, F.; Grant, E. R.; Berlinguette, C. P. PH Matters When Reducing CO_2 in an Electrochemical Flow Cell. *ACS Energy Lett.* **2020**, *5* (10), 3101–3107. https://doi.org/10.1021/acsenergylett.0c01606.